NANO LETTERS

Letter

pubs.acs.org/NanoLett

Rashba Spin–Orbit Coupling Enhanced Carrier Lifetime in $CH_3NH_3PbI_3$

Fan Zheng,[†] Liang Z. Tan,[†] Shi Liu,[‡] and Andrew M. Rappe*[,†]

[†]The Makineni Theoretical Laboratories, Department of Chemistry, University of Pennsylvania, Philadelphia, Pennsylvania 19104-6323, United States

[‡]Geophysical Laboratory Carnegie Institution for Science, Washington, D.C. 20015, United States

Supporting Information

ABSTRACT: Organometal halide perovskites are promising solar-cell materials for next-generation photovoltaic applications. The long carrier lifetime and diffusion length of these materials make them very attractive for use in light absorbers and carrier transporters. While these aspects of organometal halide perovskites have attracted the most attention, the consequences of the Rashba effect, driven by strong spin–orbit coupling, on the photovoltaic properties of these materials are largely unexplored. In this work, taking the electronic structure of $CH_3NH_3PbI_3$ (methylammonium lead iodide) as an example, we propose an intrinsic mechanism for enhanced carrier lifetime in three-dimensional (3D) Rashba materials. On the basis of first-principles calculations and a Rashba spin–orbit model, we demonstrate that the recombination rate is reduced due to the spin-forbidden transition. These results are important for understanding the fundamental physics of organometal halide perovskites and for optimizing and designing the materials with better performance. The proposed mechanism including spin degrees of freedom offers a new paradigm of using 3D Rashba materials for photovoltaic applications.

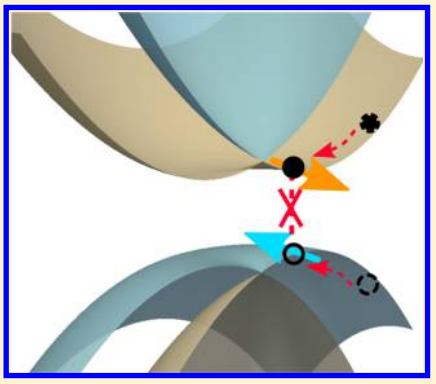

KEYWORDS: *Organometal halide perovskite, carrier lifetime, electron–phonon coupling, Rashba spin–orbit coupling, spin-forbidden transition*

The organometal halide perovskites (OMHPs) have attracted significant attention due to the rapid increase in their photovoltaic power conversion efficiency. In the past two years, the reported efficiency of OMHP-based solar cells has almost doubled from 9.7%[1] to over 20%,[2−4] making OHMPs very promising for low-cost and high-efficiency photovoltaics. $CH_3NH_3PbI_3$ ($MAPbI_3$), and other closely related hybrid perovskites such as Cl-alloyed and Br-alloyed $MAPbI_3$ ($MAPbI_{3-x}Cl_x$ and $MAPbI_{3-x}Br_x$), $(NH_2)_2CHPbI_3$ (formamidinium lead iodide, $FAPbI_3$), and Sn-alloyed $MAPbI_3$ ($MAPb_xSn_{1-x}I_3$), all display band gaps (1.1 to 2.1 eV) in the visible light region, favorable for photovoltaic applications.[5−13] The class of materials also possesses strong light absorption, fast charge generation, and high carrier mobility.[14,15] In particular, exceptionally long carrier lifetime and diffusion length have been observed in $MAPbI_3$ and $MAPbI_{3-x}Cl_x$, making them better solar cell candidates than other semiconductors with similar band gaps and absorption coefficients.[16−18]

Intense research has been directed toward understanding and further enhancing the long carrier lifetime and diffusion length in OMHPs. Previous studies reported a relatively low defect concentration in $MAPbI_3$,[19−23] which reduces the scattering centers for nonradiative charge carrier recombination. Recently, it has been suggested that the spatial carrier segregation caused by disorder-induced localization[24] or domains acting as internal p–n junctions[25−27] may reduce the recombination rate. The presence of strong spin–orbit coupling (SOC) and bulk ferroelectricity in many of the (three-dimensional) 3D Rashba OMHP materials have been studied extensively.[7,28−37] However, the direct role of spin and orbital degrees of freedom on photovoltaic applications are largely unexplored. In this work, we focus on an intrinsic mechanism for the enhancement of long carrier lifetime due to the Rashba splitting. Using first-principles calculations and effective models, we find that the Rashba splitting arising from SOC in locally polarized domains can result in spin-allowed and spin-forbidden recombination channels. The spin-forbidden recombination path has a significantly slower transition rate due to the mismatch of spin and momentum. The spin-allowed recombination path, though kinetically favorable, can be suppressed under appropriate spin texture due to the low population of free carriers induced by the fast carrier relaxation to the band edges. (Here, we consider electron–phonon scattering as the main relaxation mechanism.) Taking the electronic structures of $MAPbI_3$ under various distortions as examples, we show that the proposed mechanism is possible under room temperature and is potentially responsible for the long carrier lifetime in

Received: May 11, 2015
Revised: October 12, 2015
Published: October 13, 2015

DOI: 10.1021/acs.nanolett.5b01854
Nano Lett. 2015, 15, 7794–7800

OMHPs. This spin-dependent recombination mechanism highlights the possibility of using 3D Rashba materials[38−41] for efficient photovoltaic applications.

Figure 1 illustrates the mechanism for enhancing the carrier lifetime in a generic 3D Rashba material. The strong spin−orbit coupling effect from heavy elements (e.g., Pb, Sn, I, and Br) and inversion symmetry breaking owing to the polar distortion (e.g., aligned molecular dipoles in OMHPs) give rise to the Rashba effect, which lifts the two-fold degeneracy of bands near the band gap. This is distinct from the Dresselhaus effect, which happens in systems of different symmetry. Here, C_{4v} symmetry removes Dresselhaus splitting.[30,42] Indeed, the spin structure of the Dresselhaus model is inconsistent with density functional theory (DFT) calculations of $MAPbI_3$.[28] Near the band gap, the spin degeneracies of the conduction and valence bands are lifted, giving rise to "inner" and "outer" bands with opposite spin textures, characterizing spin rotation direction as "clockwise" ($\chi = -1$) and "counterclockwise" ($\chi = +1$) (Figure 1). The photoexcitation process creates free electrons and holes, which can quickly relax to band extrema in the presence of inelastic phonon scattering. When the spin textures of conduction band minimum (CBM) and valence band maximum (VBM) are opposite, the radiative recombination of $C_{\chi=-1} \rightarrow V_{\chi=+1}$ is a spin-forbidden transition due to the mismatch of spin states. This prevents rapid recombination as the photon-induced spin-flip is a slow process.[43] Moreover, the minimum of the $C_{\chi=-1}$ band is slightly shifted compared to the maximum of the $V_{\chi=+1}$ band (momentum mismatch). This creates an indirect band gap for recombination, which further slows down the recombination process due to the requirement of a phonon with the right momentum. This is also highlighted in ref 44, where the indirect band gap is created by the dynamic disorder of molecules. In the following, we use the terms favorable and unfavorable relative spin helicity to describe cases when the VBM and CBM have opposite and aligned spins, respectively.

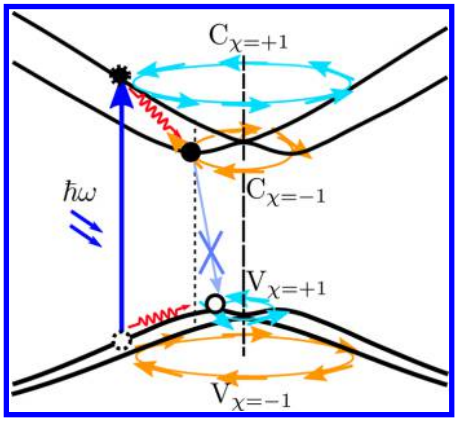

Figure 1. Diagram of Rashba bands and the electron transport path. The cyan and orange arrows indicate the directions of the spins. The spin texture χ indicates spin vortex direction with its signs characterizing spin rotation in "clockwise" ($\chi = -1$) and "counterclockwise" ($\chi = +1$). After absorbing the photons, the excited electrons on conduction bands $C_{\chi=+1}$ and $C_{\chi=-1}$ will quickly relax to $C_{\chi=-1}$ band minimum due to the inelastic phonon scattering. Similarly, the holes will quickly relax to the $V_{\chi=+1}$ band maximum. However, the radiative recombination of $C_{\chi=-1} \rightarrow V_{\chi=+1}$ is a spin-forbidden process due to the opposite spin states they have. Moreover, the minimum of $C_{\chi=-1}$ band and the maximum of $V_{\chi=+1}$ band are located in different positions in the Brillouin Zone. This creates an indirect band gap for recombination, which further slows down the recombination process.

The spin texture and carrier population of the CBM and VBM play key roles in enhancing carrier lifetime. Our first-principles DFT calculations support the realization of this mechanism in OMHPs. Taking the pseudocubic phase $MAPbI_3$ as an example, we explore the carrier dynamics after the photoexcitation. The electron−phonon coupling plays a significant role for the relaxation of the excited carriers in OMHPs.[45] Using Fermi's golden rule, we calculate the inelastic phonon scattering rate (see Methods) shown in Figure 2. The relaxation rate ($\approx 10^{15}$ s^{-1}) increases as a function of carrier energy. This is supported by the sharp jumps of the relaxation rate at frequencies corresponding to phonon modes (emission thresholds) derived mainly from the organic molecules, as shown in Figure 2. We find that the organic molecule plays an important role for carrier relaxation. The modes that are responsible for these sharp jumps are identified as MA translation, CH/NH twisting, and CH/NH stretching.[46] In particular, the contribution of these modes are found in both VBs and CBs, indicating their equally important role in electrons and holes. The scattering magnitude differences of CBs and VBs are mainly from their density of states differences (eq 4). Other modes with both MA and I vibrations also contribute to the carrier relaxations. But these modes have much lower frequencies, and the emission thresholds due to these modes occur much closer to the band edges.

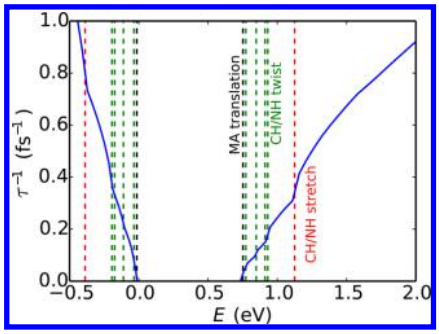

Figure 2. Dependence of phonon-induced relaxation rate on carrier energies (blue lines) for electrons (positive energies) and holes (negative energies). The VBM is located at $E = 0$ eV, and the CBM is located at $E = 0.73$ eV. The energies of phonon modes that contribute strongly to carrier relaxation are shown as dotted lines. The phonon modes listed in the graph have frequencies as 141.2 (MA translation), 315.9, 924.3, 1441.5, 1598.3 (MA twisting), and 3158.6 cm^{-1} (NH vibration), respectively. (See details in Supporting Information.)

Our calculations reveal that the phonon-induced carrier relaxation rate value is many orders of magnitude faster than the electron−hole recombination rate ($\approx 10^9$ s^{-1}).[45,47] Therefore, the carriers will rapidly thermalize and from a quasi-static equilibrium distribution near the CBM and VBM. In Rashba SOC bands, the special spin configuration always allows a carrier of a certain spin to relax to a lower energy state of the same spin via the emission of a finite-wavevector phonon. A sequence of such emission events results in the relaxation of carriers to band edges. In the ideal case of low temperatures and large Rashba splitting, nearly all free carriers are located at the band extrema, and the effects of spin and momentum mismatch on the enhancement of the carrier lifetime will be the greatest. This effect is less strong at finite temperatures and small Rashba splitting because of the thermal occupation of

DOI: 10.1021/acs.nanolett.5b01854
Nano Lett. 2015, 15, 7794−7800

$C_{\chi=1}$ and $V_{\chi=-1}$ bands, which opens spin-allowed recombination paths such as $C_{\chi=-1} \rightarrow V_{\chi=-1}$. In the case of favorable relative spin helicity, we investigate this temperature effect by examining the Rashba splitting using a Rashba Hamiltonian[48]

$$H_R = \frac{\hbar^2 k^2}{2m} + \hbar v_R \hat{z} \times \vec{k} \cdot \vec{\sigma} \quad (1)$$

$$E_{k,\sigma} = \frac{\hbar^2 (k_z^2 + k_\perp^2)}{2m} + \sigma \hbar v_R k_\perp,\ k_\perp = \sqrt{k_x^2 + k_y^2} \quad (2)$$

The parameters m and v_R represent the band mass and Rashba interaction, respectively. By fitting m and v_R to DFT band structure of fully relaxed $MAPbI_3$ pseudocubic lattice, the band energies and spin configurations of the model agree with DFT calculated results. Furthermore, the tight-binding model introduced below and in the Supporting Information can be reduced to this Rashba Hamiltonian, demonstrating the role of Rashba SOC in $MAPbI_3$. We find that the conduction band Rashba splitting (0.108 eV) is much larger than the thermal energy scale, while the valence band Rashba splitting (0.016 eV) is comparable to the thermal energy scale. Because electronic correlations are not fully captured in DFT,[13] these values are likely lower bounds of the true splitting. These relatively large Rashba splittings are likely to give rise to a significant enhancement in carrier lifetime even at room temperature.

There is an additional factor, arising from the unique features of Rashba band structure, which promotes occupation of the band extrema. In contrast to the band extrema of ordinary parabolic bands in semiconductors that are points in momentum space, those of Rashba materials are one-dimensional rings (Figure 1). This leads to an increase in the density of states at low energies, resulting in a population of carriers heavily skewed toward the band extrema (Figure 3a,b) and consequently reduces the overall recombination rate due to the reasons of spin and momentum mismatch as discussed above. This increased density of states leads to a predominance of desirable spin carriers, even though the valence band splitting is comparable to the room-temperature energy scale, protecting the long carrier lifetimes even at room temperature.

The magnitude of Rashba splitting depends on the amount of polar distortion and the strength of the SOC, both of which can be captured by the Rashba velocity parameter v_R. We calculate the averaged recombination rate

$$\langle \tau^{-1} \rangle = \sum_{\chi,\chi'} \frac{\int d^3k \tau^{-1}_{\chi,\chi'}(k) n^e_\chi(k) n^h_{\chi'}(k)}{\int d^3k n^e_\chi(k) n^h_{\chi'}(k)} \quad (3)$$

where $\tau^{-1}_{\chi,\chi'}(k) = B_{\chi,\chi'}\, n^e_\chi(k)\, n^h_{\chi'}(k)$ is the band- and momentum-resolved recombination rate. The spin-mismatch effect is captured by the rate constant $B_{\chi,\chi'}$, which is larger when χ and χ' have parallel spins than otherwise. Enhancement of density of states enters via the temperature dependent electron and hole occupation numbers $n^e(k)$ and $n^h(k)$, which tend to peak at different k-points because of momentum mismatch. In order to quantify the effect of Rashba splitting on the recombination rate, we define the unitless lifetime enhancement factor as the ratio $\langle \tau^{-1} \rangle_{v_R=0} / \langle \tau^{-1} \rangle_{v_R}$, where $\langle \tau^{-1} \rangle_{v_R}$ is the average recombination rate when SOC is taken into account, and $\langle \tau^{-1} \rangle_{v_R=0}$ refers to a calculation where SOC is explicitly set to zero in the Rashba model (Figure 3c). Upon tuning the Rashba splitting continuously in our model, we find that the lifetime enhancement factor increases approximately exponentially with Rashba splitting, a consequence of the exponential behavior of carrier occupation numbers near the tail of the Fermi–Dirac distribution. Our model predicts that a Rashba splitting of 0.1 eV can give rise to an order of magnitude enhancement of carrier lifetime.

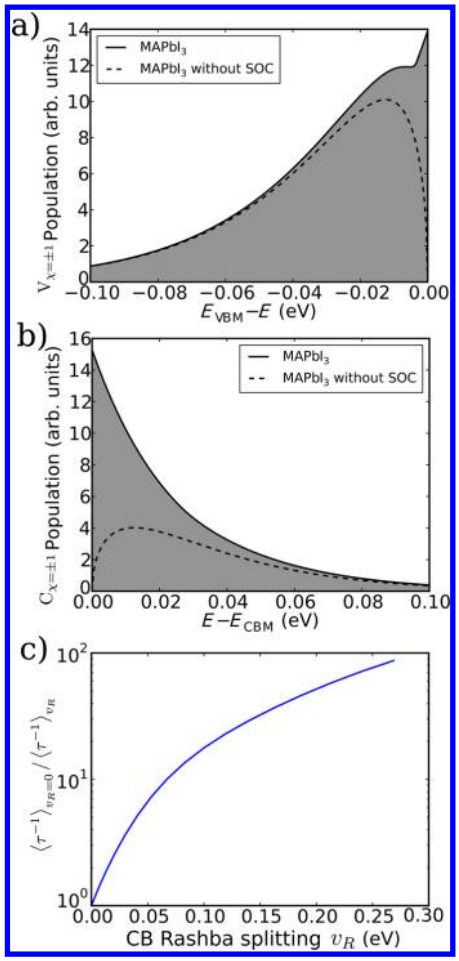

Figure 3. Population of carriers at T = 298 K, calculated from the Fermi–Dirac distribution, for (a) the top valence band and (b) the bottom conduction band of $MAPbI_3$. Shown in dashed lines are the population of carriers in a model material with the same band masses as $MAPbI_3$ but with vanishing Rashba splitting. (c) Unitless lifetime enhancement factor, as defined in the text, as a function of the conduction band Rashba splitting energy.

As we have seen, the favorable spin helicity of the VBM and the CBM enables the intrinsic enhancement of carrier lifetime with the amount of enhancement depending on the magnitude of the Rashba splitting. The inversion symmetry-breaking distortions that influence relative spin helicity and splitting magnitude are therefore intimately related to the SOC enhancement of carrier lifetime. To reveal the relation, we start with a tight binding model of the inorganic PbI_3^- lattice (see Methods). The displacements of Pb atoms along the z-direction give rise to effective hoppings between Pb s- and p-orbitals along the equatorial direction (Figure 4a), which would vanish by symmetry in the absence of such displacements. Similarly, displacement of the apical I atoms along the z-direction changes Pb–I bond lengths and effective hoppings along the apical direction (Figure 4b). These modifications of hopping parameters create the effective inversion symmetry breaking electric fields described by $\hbar v_R$ in our low-energy

DOI: 10.1021/acs.nanolett.5b01854
Nano Lett. 2015, 15, 7794–7800

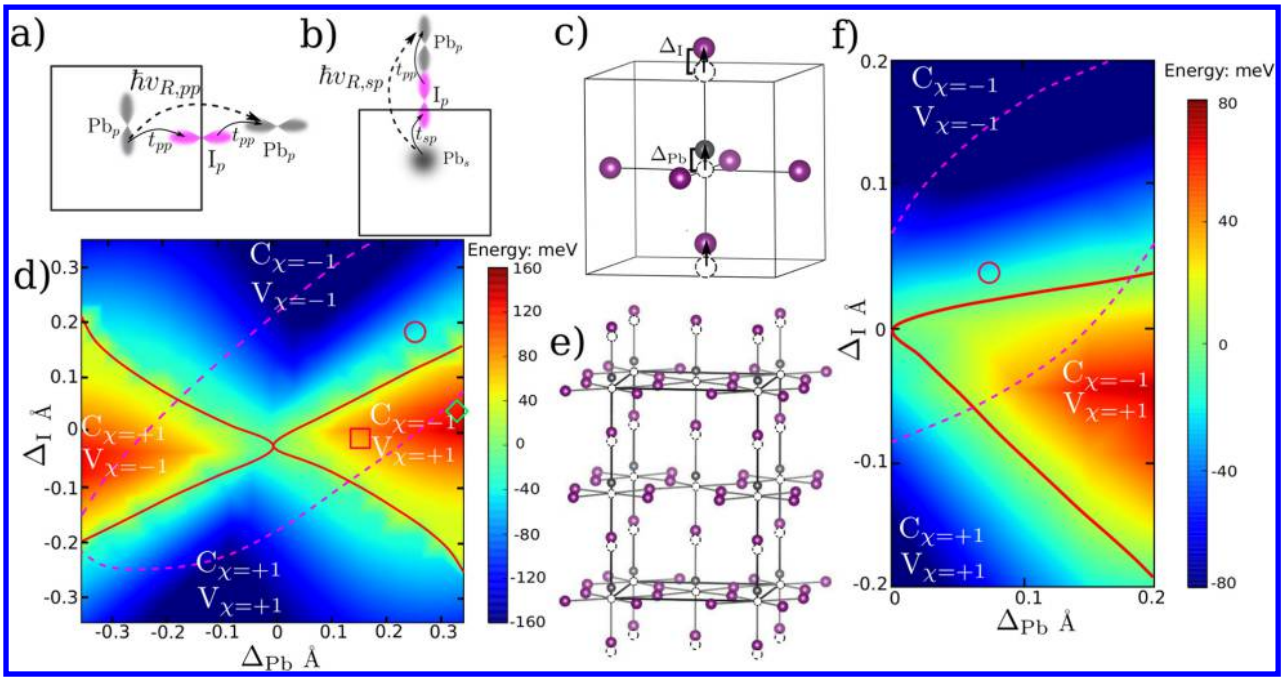

Figure 4. (a,b) Hopping schemes illustrate the effective electric field $\hbar v_{R,pp}$ and $\hbar v_{R,sp}$ created by horizontal hopping and vertical hopping respectively for a range of Pb and I displacements. These two factors caused by different Pb and I displacements controls spin textures of CBM and VBM differently, giving rise to different spin helicities. (c) Schematic diagram showing Pb and I displacement in pseudocubic $MAPbI_3$. Pb, silver. I, indigo. Broken circles are original high-symmetry positions. Molecules are not shown here. (d) Phase diagram of splitting energy and spin texture for structures with different Pb and apical I displacement in pseudocubic $MAPbI_3$ calculated from DFT. The color is the minimum value between the averaged splitting energy of two Rashba conduction bands and two valence bands (see Methods). The spin texture phase boundaries are indicated by the solid red lines. When the structure transforms from a favorable spin texture region to an unfavorable spin texture region, the two Rashba valence bands or conduction bands exchange, creating negative splitting energy. The dashed lines indicate the areas with energy cost less than 25 meV (under room-temperature fluctuation) to distort Pb and I. The red square/green diamond indicate the displacements of Ti and apical O of $BaTiO_3$/$PbTiO_3$ for comparison.[68,69] The red circle marks the distortions with the lowest total energy. (e) Schematic diagram showing Pb and I displacement in tetragonal $MAPbI_3$. (f) Similar to d, phase diagram of splitting energy and spin texture for structures with different Pb and apical I displacement in tetragonal $MAPbI_3$ calculated from DFT. The red circle marks the distortions with the lowest total energy.

theory model (eq 1). In this model, we find that the spin textures of the valence bands and conduction bands depend on the combination of Pb and I displacements. By shifting Pb and I atoms, we can control the spin textures of the valence and conduction bands, creating favorable and unfavorable relative spin helicities. As we now proceed to show, this picture is confirmed with DFT calculations.

We focus on two phases of $MAPbI_3$, pseudocubic phase (α-phase) and tetragonal phase (β-phase).[11] The pseudocubic phase of $MAPbI_3$ has space group $P4mm$ with $a = b = 6.31$ Å and $c = 6.32$ Å. It does not have inversion symmetry, because of the permanent dipole moments of MA^+. It is suggested that the aligned molecular orientations in polar domain can drive Pb−I displacement giving rise to ferroelectric distortions.[49] The DFT fully relaxed pseudocubic structure at 0 K is monoclinic with molecular dipole pointing to the face center of PbI_3^- sublattice (see Supporting Information). Because this 0 K structure is of limited use in the discussion of the PbI_3^- sublattice distortions at finite temperature, here we explore all the possible structures with Pb and apical I displacements along c-direction while respecting the space group. Without distorting the PbI_3^- sublattice, the electronic effect of molecular permanent dipole moment to Rashba splitting is negligible. Thus, the molecules are aligned along c-direction for simplicity. Shown in Figure 4d are the DFT-calculated spin textures and averaged Rashba splittings at VBM and CBM respectively for a given pair of Pb and I displacements (see Methods). The areas outlined by the solid red lines indicate the structures with favorable relative spin helicities, which also have relatively large band splittings. We find that these structures have Pb and apical I displaced along opposite directions. This is consistent with typical ferroelectric distortions in inorganic ferroelectrics such as $BaTiO_3$ and $PbTiO_3$. It is noted that large apical I displacement tends to drive the system away from the region with favorable relative spin helicity to unfavorable spin helicity (Figure 4d).

We further explore the relationship between relative spin helicity and local distortions in tetragonal $MAPbI_3$,[11] which is observed at room temperature. The space group of the tetragonal phase is identified as $I4cm$, allowing both ferroelectric distortion and PbI_6 octahedral rotation (Figure 4e). Figure 4f shows the spin textures and the averaged Rashba splitting for different Pb and I displacements in $I4cm$ space group. The tetragonal phase exhibits similar displacement-helicity relationship to the cubic phase, indicating that the Rashba splitting can also enhance the carrier lifetime in tetragonal phase.

Various experimental studies have demonstrated switchable ferroelectric domains (~100 nm) and ferroelectricity at room temperature.[50−53] Many theoretical studies also suggested the existence of local polar regions at room temperature.[24,26,54,55] The atomic structures of these polar regions are still not clear. Energetically accessible structures at room temperature are highlighted by dashed red lines in Figure 4d,f, which cover a large region displaying favorable spin textures. Hence, our proposed mechanism can be realized in $MAPbI_3$ at room temperature and provides a possible explanation of long carrier

DOI: 10.1021/acs.nanolett.5b01854
Nano Lett. 2015, 15, 7794−7800

lifetime. Molecular dynamics and Monte Carlo simulation[12,56,57] suggest that the molecule can rotate in a relatively short time scale, which may result in dynamic disorder although the issue of order and disorder is still an open question. However, our proposed mechanism is expected to be valid as long as the disorder correlation length is large enough to create local regions of finite Rashba splitting (see details in Supporting Information). In these local regions, we expect that our mechanism still contribute to the carrier lifetime enhancement. This is also supported by many studied listed above as they show large polarized domains to validate this mechanism. Moreover, recent studies of carrier dynamics under magnetic field illustrate the significance of spin in carrier recombinations.[58−60]

Rashba SOC enhanced carrier lifetime highlights the potential of 3D Rashba materials[61] for photovoltaic applications. The ability to incorporate different organic molecules in OMHPs provides a robust avenue to design 3D Rashba materials. If changes are made to the dipole magnitude of organic molecules in halide perovskite, the spin helicities and band splittings are likely to be affected via the Pb and I displacements as discussed above. Conventional experimental techniques of controlling bulk polarization (e.g, epitaxial strain) can also be applied to optimize power conversion efficiency.

In summary, we have proposed an intrinsic mechanism for enhancing carrier lifetime in 3D Rashba materials. In the case of OMHPs, such mechanism can be realized by the joint action of molecules (electron−phonon coupling) and PbI_3^- sublattices (giving rise to spin−orbit coupling). The photoexcited carriers quickly relax to band edges due to the electron−phonon coupling. When the spin textures for CBM and VBM are opposite, the Rashba splitting of bands close to the band gap results in spin-allowed and spin-forbidden recombination paths. The spin-forbidden recombination path has slow transition rate due to mismatch of spin and momentum. The spin-allowed recombination path, though kinetically favorable, will only influence a smaller amount of carriers. In order to achieve this favorable spin helicity, we explore different Pb and I displacement giving rise to different spin textures. A tight binding model is developed to explain this spin-displacement relation. This mechanism allows OMHPs to behave like direct-gap semiconductors upon photoexcitation and like indirect-gap semiconductors during radiative recombination, simultaneously harnessing the large carrier densities of the former and the long lifetimes of the latter. The mechanism we propose highlights the importance of the Rashba effect and structural distortion for achieving long carrier lifetime and consequently long diffusion length in organometal halide perovskites.

Methods. *DFT and Electron−Phonon Coupling.* The plane-wave DFT package QUANTUM-ESPRESSO[62] with the Perdew−Burke−Ernzerhof[63] functional (PBE) is used to perform electronic structure and electron−phonon coupling calculation. Norm-conserving, designed nonlocal pseudopotentials were generated with the OPIUM package.[64,65] The following orbitals are pseudized and considered as valence electrons: Pb, 5d, 6s, 6p; I, 4d, 5s, 5p; C, 2s, 2p; N, 2s, 2p; H, 1s. The planewave cutoff is 50 Ryd to get converged charge density. The k-points are chosen as 8 × 8 × 8 Monkhorst−Pack grid for pseudocubic structure and 6 × 6 × 4 for tetragonal structure.[49] As also shown in other work, the band gap is underestimated with PBE+SOC.[7,29,31,33−36] We calculate the inelastic phonon scattering rate for electrons and holes using Fermi's golden rule (with SOC included)[45,66]

$$\tau_{k,n\to n'}^{(\mathrm{ph})-1} = \hbar^{-1}\frac{V}{(2\pi)^3}\sum_{\nu}\int d^3k' |g_{\nu,k,k'}^{n,n'}|^2 \delta(E_{k,n} - E_{k',n'} - \hbar\omega_\nu) \quad (4)$$

where k and n are the wavevector and band index respectively, ν denotes the phonon mode, $E_{k,n}$ are electronic band energies and V is the volume of the unit cell. The phonon frequencies ω_ν and electron−phonon matrix elements $g_{\nu,k,k'}^{n,n'}$ are obtained from density functional perturbation theory.[67] Further details are included in Supporting Information.

Lifetime Enhancement Factor. The rate constant $B_{\chi\chi'}$ in eq 3 of spin-allowed ($\chi = \chi' = \pm 1$) and spin-forbidden ($\chi \neq \chi'$) transitions are obtained from averaged DFT calculated oscillator strength over the k points near band edges. For example, $B_{1,1} \approx 3.7B_{1,-1}$. Although the calculation with PBE+SOC underestimated the band gap, in this case only the ratio of spin-allowed and spin-forbidden transitions matters. In this work, the oscillator strength is used to show transition probability. Because spin-allowed and spin-forbidden transitions occur at similar energies (around the magnitude of band gap), the ratio of oscillator strength between these two types of transitions are not affected significantly.

Tight-Binding Model. The tight-binding model is based on PbI_3^- structure. Pb 6s, Pb 6p and the I 5p orbitals are included in this model with spin degree of freedom. The tight-binding Hamiltonian is

$$H_{\mathrm{TB}} = H_{\mathrm{hop}} + H_{\mathrm{SOC}} \quad (5)$$

where H_{hop} considers the nearest neighbor hopping between two orbitals, described by t_{sp}, $t_{\mathrm{pp}\sigma}$, and $t_{\mathrm{pp}\pi}$ for s−p σ hopping, p−p σ hopping, and p−p π hopping, respectively. H_{SOC} is the on-site SOC term defined as $\lambda_{\mathrm{Rashba}}\mathbf{L}\cdot\mathbf{S}$. Hopping parameters and $\lambda_{\mathrm{Rashba}}$ are fitted to DFT band structures of pseudocubic $MAPbI_3$ with experimental lattice constants. We reduce our tight-binding Hamiltonian into the Rashba effective model (eq 1) in two steps, following the procedure outlined in.[28] First, the I p orbitals are removed by projecting H_{TB} to the subspace of Pb orbitals

$$H_{\mathrm{Pb}} = \mathcal{P}H_{\mathrm{TB}}\mathcal{P} + \mathcal{P}H_{\mathrm{TB}}Q\frac{1}{E - QH_{\mathrm{TB}}Q}QH_{\mathrm{TB}}\mathcal{P} \quad (6)$$

where $\mathcal{P}$ and Q are projection operators to the Pb and I subspaces, respectively. This results in an effective Hamiltonian H_{Pb} containing inversion symmetry breaking terms which modify the effective hopping between Pb orbitals.[28] Next, H_{Pb} is reduced to H_{R} using a similar projection to the CBM and VBM. (See details in Supporting Information.)

Rashba Splitting Energy Phase Diagram. For both pseudocubic and tetragonal phases of $MAPbI_3$, the apical I and Pb atoms are displaced while respecting the space group identified from experiments. These displacements generate the 2D map (Figure 4) and each point in this 2D map corresponds to one structure with the specific pair of Pb and I displacements. The Rashba splitting energy is defined as $|\Delta E^{\mathrm{R}}| = \min[\langle E_{\mathrm{C,s=CBM+1}} - E_{\mathrm{C,s=CBM}}\rangle, \langle E_{\mathrm{V,s=VBM}} - E_{\mathrm{V,s=VBM-1}}\rangle]$. Here, the sign of ΔE^{R} is indicated as +1 for favorable spin helicity, and −1 for unfavorable spin helicity. "⟨ ⟩" indicates the average over k-points near CBM or VBM.

■ ASSOCIATED CONTENT

Supporting Information

The Supporting Information is available free of charge on the ACS Publications website at DOI: 10.1021/acs.nanolett.5b01854.

DOI: 10.1021/acs.nanolett.5b01854
Nano Lett. 2015, 15, 7794−7800

Atomic coordinates of the structures used in the calculations; detailed descriptions of the electron−phonon coupling calculation, phonon modes contributing to the carriers relaxation, numerical tight-binding model fitting, and spin-dependent oscillator strength; derivation of the Rashba Hamiltonian based on the tight-binding model; and discussion of the Rashba model in the presence of disorder. (PDF)

AUTHOR INFORMATION

Corresponding Author

*E-mail: rappe@sas.upenn.edu.

Notes

The authors declare no competing financial interest.

ACKNOWLEDGMENTS

F.Z. was supported by the Department of Energy under Grant DE-FG02-07ER46431. L.Z.T. was supported by the Office of Naval Research under Grant N00014-14-1-0761. S.L. was supported by the National Science Foundation under Grant CBET-1159736 and the Carnegie Institution for Science. A.M.R. was supported by the National Science Foundation under Grant DMR-1120901. The authors acknowledge computational support from the HPCMO of the DOD and the NERSC center of the DOE.

REFERENCES

(1) Kim, H.-S.; Lee, C.-R.; Im, J.-H.; Lee, K.-B.; Moehl, T.; Marchioro, A.; Moon, S.-J.; Humphry-Baker, R.; Yum, J.-H.; Moser, J. E.; Grätzel, M.; Park, N.-G. *Sci. Rep.* **2012**, *2*, 591−597.

(2) Zhou, H.; Chen, Q.; Li, G.; Luo, S.; Song, T.-b.; Duan, H.-S.; Hong, Z.; You, J.; Liu, Y.; Yang, Y. *Science* **2014**, *345*, 542−546.

(3) Jeon, N. J.; Lee, H. G.; Kim, Y. C.; Seo, J.; Noh, J. H.; Lee, J.; Seok, S. I. *J. Am. Chem. Soc.* **2014**, *136*, 7837−7840.

(4) NREL. Research Cell Efficiency Records; http://www.nrel.gov/ncpv/images/efficiency_chart.jpg (accessed Oct. 11, 2015).

(5) Papavassiliou, G. C.; Koutselas, I. *Synth. Met.* **1995**, *71*, 1713−1714.

(6) Noel, N. K.; Stranks, S. D.; Abate, A.; Wehrenfennig, C.; Guarnera, S.; Haghighirad, A.; Sadhanala, A.; Eperon, G. E.; Pathak, S. K.; Johnston, M. B.; Petrozza, A.; Herz, L. M.; Snaith, H. J. *Energy Environ. Sci.* **2014**, *7*, 3061−3068.

(7) Umari, P.; Mosconi, E.; De Angelis, F. *Sci. Rep.* **2014**, *4*, 4467-1−4467-7.

(8) Chiarella, F.; Zappettini, A.; Licci, F.; Borriello, I.; Cantele, G.; Ninno, D.; Cassinese, A.; Vaglio, R. *Phys. Rev. B: Condens. Matter Mater. Phys.* **2008**, *77*, 045129.

(9) Ogomi, Y.; Morita, A.; Tsukamoto, S.; Saitho, T.; Fujikawa, N.; Shen, Q.; Toyoda, T.; Yoshino, K.; Pandey, S. S.; Ma, T.; Hayase, S. *J. Phys. Chem. Lett.* **2014**, *5*, 1004−1011.

(10) Eperon, G. E.; Stranks, S. D.; Menelaou, C.; Johnston, M. B.; Herz, L. M.; Snaith, H. J. *Energy Environ. Sci.* **2014**, *7*, 982−988.

(11) Stoumpos, C. C.; Malliakas, C. D.; Kanatzidis, M. G. *Inorg. Chem.* **2013**, *52*, 9019−9038.

(12) Mosconi, E.; Quarti, C.; Ivanovska, T.; Ruani, G.; De Angelis, F. *Phys. Chem. Chem. Phys.* **2014**, *16*, 16137−16144.

(13) Filip, M. R.; Giustino, F. *Phys. Rev. B: Condens. Matter Mater. Phys.* **2014**, *90*, 245145.

(14) Ponseca, J.; Carlito, S.; Savenije, T. J.; Abdellah, M.; Zheng, K.; Yartsev, A.; Pascher, T.; Harlang, T.; Chabera, P.; Pullerits, T.; Stepanov, A.; Wolf, J.-P.; Sundstrom, V. *J. Am. Chem. Soc.* **2014**, *136*, 5189−5192.

(15) Edri, E.; Kirmayer, S.; Mukhopadhyay, S.; Gartsman, K.; Hodes, G.; Cahen, D. *Nat. Commun.* **2014**, *5*, 3461−3468.

(16) Xing, G.; Mathews, N.; Sun, S.; Lim, S. S.; Lam, Y. M.; Graetzel, M.; Mhaisalkar, S.; Sum, T. C. *Science* **2013**, *342*, 344−347.

(17) Stranks, S. D.; Eperon, G. E.; Grancini, G.; Menelaou, C.; Alcocer, M. J.; Leijtens, T.; Herz, L. M.; Petrozza, A.; Snaith, H. J. *Science* **2013**, *342*, 341−344.

(18) Wehrenfennig, C.; Eperon, G. E.; Johnston, M. B.; Snaith, H. J.; Herz, L. M. *Adv. Mater.* **2014**, *26*, 1584−1589.

(19) Kim, J.; Lee, S.-H.; Lee, J. H.; Hong, K.-H. *J. Phys. Chem. Lett.* **2014**, *5*, 1312−1317.

(20) Yin, W.-J.; Shi, T.; Yan, Y. *Appl. Phys. Lett.* **2014**, *104*, 063903.

(21) Du, M. H. *J. Mater. Chem. A* **2014**, *2*, 9091−9098.

(22) Yamada, Y.; Endo, M.; Wakamiya, A.; Kanemitsu, Y. *J. Phys. Chem. Lett.* **2015**, *6*, 482−486.

(23) Buin, A.; Pietsch, P.; Xu, J.; Voznyy, O.; Ip, A. H.; Comin, R.; Sargent, E. H. *Nano Lett.* **2014**, *14*, 6281−6286.

(24) Ma, J.; Wang, L.-W. *Nano Lett.* **2015**, *15*, 248−253.

(25) Frost, J. M.; Butler, K. T.; Walsh, A. *APL Mater.* **2014**, *2*, 081506−081515.

(26) Frost, J. M.; Butler, K. T.; Brivio, F.; Hendon, C. H.; van Schilfgaarde, M.; Walsh, A. *Nano Lett.* **2014**, *14*, 2584−2590.

(27) Liu, S.; Zheng, F.; Koocher, N. Z.; Takenaka, H.; Wang, F.; Rappe, A. M. *J. Phys. Chem. Lett.* **2015**, *6*, 693−699.

(28) Kim, M.; Im, J.; Freeman, A. J.; Ihm, J.; Jin, H. *Proc. Natl. Acad. Sci. U. S. A.* **2014**, *111*, 6900−6904.

(29) Even, J.; Pedesseau, L.; Jancu, J.-M.; Katan, C. *J. Phys. Chem. Lett.* **2013**, *4*, 2999−3005.

(30) Stroppa, A.; Di Sante, D.; Barone, P.; Bokdam, M.; Kresse, G.; Franchini, C.; Whangbo, M.-H.; Picozzi, S. *Nat. Commun.* **2014**, *5*, 5900−5907.

(31) Amat, A.; Mosconi, E.; Ronca, E.; Quarti, C.; Umari, P.; Nazeeruddin, M. K.; Graetzel, M.; De Angelis, F. *Nano Lett.* **2014**, *14*, 3608−3616.

(32) Even, J.; Pedesseau, L.; Jancu, J.-M.; Katan, C. *Phys. Status Solidi RRL* **2014**, *8*, 31−35.

(33) Menéndez-Proupin, E.; Palacios, P.; Wahnón, P.; Conesa, J. *Phys. Rev. B: Condens. Matter Mater. Phys.* **2014**, *90*, 045207−045213.

(34) Brivio, F.; Butler, K. T.; Walsh, A.; van Schilfgaarde, M. *Phys. Rev. B: Condens. Matter Mater. Phys.* **2014**, *89*, 155204.

(35) Zhu, X.; Su, H.; Marcus, R. A.; Michel-Beyerle, M. E. *J. Phys. Chem. Lett.* **2014**, *5*, 3061−3065.

(36) Kim, J.; Lee, S.-C.; Lee, S.-H.; Hong, K.-H. *J. Phys. Chem. C* **2015**, *119*, 4627−4634.

(37) Kepenekian, M.; Robles, R.; Katan, C.; Sapori, D.; Pedesseau, L.; Even, J. *ACS Nano* **2015**, DOI: 10.1021/acsnano.5b04409.

(38) Krempaský, J.; Volfová, H.; Muff, S.; Pilet, N.; Landolt, G.; Radović, M.; Shi, M.; Kriegner, D.; Holý, V.; Braun, J. et al. 2015, arXiv:1503.05004.

(39) Zhong, Z.; Si, L.; Zhang, Q.; Yin, W.-G.; Yunoki, S.; Held, K. *Adv. Mater. Interfaces* **2015**, *2*, 1400445-1−1400445-5.

(40) Picozzi, S. *Front. Phys.* **2014**, *2*, 1−5.

(41) Yuan, H.; Wang, X.; Lian, B.; Zhang, H.; Fang, X.; Shen, B.; Xu, G.; Xu, Y.; Zhang, S.-C.; Hwang, H. Y.; Cui, Y. *Nat. Nanotechnol.* **2014**, *9*, 851−857.

(42) Winkler, R. *Spin-orbit Coupling Effects in Two-Dimensional Electron and Hole Systems*; Springer Tracts in Modern Physics, 3rd ed.; Springer, 2003; Vol *191*.

(43) Liu, S.; Srinivasan, S.; Tao, J.; Grady, M. C.; Soroush, M.; Rappe, A. M. *J. Phys. Chem. A* **2014**, *118*, 9310−9318.

(44) Motta, C.; Mellouhi, F. E.; Kais, S.; Tabet, N.; Alharbi, F.; Sanvito, S. *Nat. Commun.* **2015**, *6*, 7026.

(45) Kawai, H.; Giorgi, G.; Marini, A.; Yamashita, K. *Nano Lett.* **2015**, *15*, 3103−3108.

(46) Quarti, C.; Grancini, G.; Mosconi, E.; Bruno, P.; Ball, J. M.; Lee, M. M.; Snaith, H. J.; Petrozza, A.; Angelis, F. D. *J. Phys. Chem. Lett.* **2014**, *5*, 279−284.

(47) Filippetti, A.; Delugas, P.; Mattoni, A. *J. Phys. Chem. C* **2014**, *118*, 24843−24853.

(48) Bychkov, Y. A.; Rashba, E. *JETP Lett.* **1984**, *39*, 78−81.

(49) Zheng, F.; Takenaka, H.; Wang, F.; Koocher, N. Z.; Rappe, A. M. *J. Phys. Chem. Lett.* **2015**, *6*, 31−37.

DOI: 10.1021/acs.nanolett.5b01854
Nano Lett. 2015, 15, 7794−7800

(50) Kutes, Y.; Ye, L.; Zhou, Y.; Pang, S.; Huey, B. D.; Padture, N. P. *J. Phys. Chem. Lett.* **2014**, *5*, 3335−3339.
(51) Chen, B.; Shi, J.; Zheng, X.; Zhou, Y.; Zhu, K.; Priya, S. *J. Mater. Chem. A* **2015**, *3*, 7699−7705.
(52) Kim, H. S.; Kim, S. K.; Kim, B. J.; Shin, K.-S.; Kumar, M. G.; Jung, H. S.; Kim, S.-W.; Park, N.-G. *J. Phys. Chem. Lett.* **2015**, *6*, 1729−1735.
(53) Coll, M.; Gomez, A.; Mas-Marza, E.; Almora, O.; Garcia-Belmonte, G.; Campoy-Quiles, M.; Bisquert, J. *J. Phys. Chem. Lett.* **2015**, *6*, 1408−1413.
(54) Quarti, C.; Mosconi, E.; De Angelis, F. *Chem. Mater.* **2014**, *26*, 6557−6569.
(55) Goehry, C.; Nemnes, G. A.; Manolescu, A. *J. Phys. Chem. C* **2015**, *119*, 19674−19680.
(56) Quarti, C.; Mosconi, E.; Angelis, F. D. *Phys. Chem. Chem. Phys.* **2015**, *17*, 9394−9409.
(57) Leguy, A. M.; Frost, J. M.; McMahon, A. P.; Sakai, V. G.; Kochelmann, W.; Law, C.; Li, X.; Foglia, F.; Walsh, A.; Regan, B. C.; Nelson, J.; Cabral, J. T.; Barnes, P. R. *Nat. Commun.* **2015**, *6*, 7124.
(58) Giovanni, D.; Ma, H.; Chua, J.; Grätzel, M.; Ramesh, R.; Mhaisalkar, S.; Mathews, N.; Sum, T. C. *Nano Lett.* **2015**, *15*, 1553−1558.
(59) Hsiao, Y.-C.; Wu, T.; Li, M.; Hu, B. *Adv. Mater.* **2015**, *27*, 2899−2906.
(60) Zhang, C.; Sun, D.; Sheng, C.-X.; Zhai, Y. X.; Mielczarek, K.; Zakhidov, A.; Vardeny, Z. V. *Nat. Phys.* **2015**, *11*, 427−434.
(61) Das, T.; Balatsky, A. V. *Nat. Commun.* **2013**, *4*, 1972−1978.
(62) Giannozzi, P.; Baroni, S.; Bonini, N.; Calandra, M.; Car, R.; Cavazzoni, C.; Ceresoli, D.; Chiarotti, G. L.; Cococcioni, M.; D, I.; et al. *J. Phys.: Condens. Matter* **2009**, *21*, 395502−395520.
(63) Perdew, J. P.; Burke, K.; Ernzerhof, M. *Phys. Rev. Lett.* **1996**, *77*, 3865−3868.
(64) Rappe, A. M.; Rabe, K. M.; Kaxiras, E.; Joannopoulos, J. D. *Phys. Rev. B: Condens. Matter Mater. Phys.* **1990**, *41*, 1227−1230.
(65) Ramer, N. J.; Rappe, A. M. *Phys. Rev. B: Condens. Matter Mater. Phys.* **1999**, *59*, 12471−12478.
(66) Bernardi, M.; Vigil-Fowler, D.; Lischner, J.; Neaton, J. B.; Louie, S. G. *Phys. Rev. Lett.* **2014**, *112*, 257402−257406.
(67) Baroni, S.; de Gironcoli, S.; Dal Corso, A. *Rev. Mod. Phys.* **2001**, *73*, 515−562.
(68) Wäsche, R.; Denner, W.; Schulz, H. *Mater. Res. Bull.* **1981**, *16*, 497−500.
(69) Ivanov, S.; Tellgren, R.; Porcher, F.; Ericsson, T.; Mosunov, A.; Beran, P.; Korchagina, S.; Kumar, P. A.; Mathieu, R.; Nordblad, P. *Mater. Res. Bull.* **2012**, *47*, 3253−3268.

DOI: 10.1021/acs.nanolett.5b01854
Nano Lett. 2015, 15, 7794−7800